Optical Properties and Optimization of LaB_6 Thin Films for Photothermal Applications

Ramu Pasupathi Sugavaneshwar[1,2], Ørjan Sele Handegård[1,3], Anh Tung Doan[1,3], Thien Duc Ngo[1,3], Toan Phuoc Tran[1,3], Hai Dang Ngo[1,3], Thang Duy Dao[1], Satoshi Ishii[1], Shigeki Otani[1,4], and Tadaaki Nagao[1,3,*]

[1]International Center for Materials Nanoarchitectonics (WPI-MANA), National Institute for Materials Science (NIMS), 1-1 Namiki, Tsukuba, Ibaraki 305-0044, Japan

[2]VIT Bhopal University, Bhopal-Indore highway, Kothrikalan, Sehore, Madhya Pradesh- 466114, India

[3]Department of Condensed Matter Physics Graduate School of Science, Hokkaido University, Kita-10 Nishi-8 Kita-ku, Sapporo 060-0810, Japan

[4]Research Center for Functional Materials, National Institute for Materials Science (NIMS), 1-1 Namiki, Tsukuba, Ibaraki 305-0044, Japan

*Corresponding Author: NAGAO.Tadaaki@nims.go.jp

Abstract

We report the growth of highly crystalline LaB_6 films with excellent optical response and low loss, which will be useful for high-performance photothermal device applications when combined with their inherent refractory properties. Optimum growth parameters for realizing uniaxial and coherent LaB_6 thin films, exhibiting an excellent plasmonic response for near- to mid-infrared device applications, were established. Numerical electromagnetic simulations of the LaB_6 nanostructures revealed that the electromagnetic field at the LaB_6 surface could be as high as that of the Au nanostructures. Furthermore, the LaB_6 nanostructures show resonance in the visible (red) to mid-infrared region comparable to those of Au with the added advantage of improved temperature stability that can withstand harsh photothermal device operations.

1 Introduction

Research activities in the field of plasmonics are steadily growing in number and gaining increased attention from the interdisciplinary research field of photoenergy harvesting and sensing applications [1-6]. Noble metals or coinage metals, such as Au, Ag, Cu, and Al, have been extensively investigated since the early stage of plasmonics research during the 1990s owing to their excellent plasmonic response and remarkable device performance in sensing applications. The strong demand for applying plasmonic

devices in harsher environments [7-9] such as in plasmon-enhanced photocatalysis [10], photothermal nanoconverters [9], thermophotovoltaics [11, 12], and heat-assisted magnetic recording (HAMR) [13-17] has recently triggered the exploration of more robust plasmonic ceramics and shown a significant impact across a broad spectrum of studies. Several of these applications demand high-temperature operation that traditional plasmonic materials such as Ag, Au, and Al cannot withstand despite offering superior optical performance.

As plasmonic research starts to cover such practical applications, from a material synthesis perspective, it is becoming necessary to find new classes of materials, optimize their properties when adapted to specific applications, and further explore new functionalities. For example, indium tin oxide (ITO) and TiN are robust ceramic plasmonic materials used in certain applications under difficult operating conditions [13-18]. However, they also degrade performance in high-temperature operations owing to accelerated oxidation above 400 °C [19]. In this context, LaB_6 can be an excellent candidate and is a known material for use in thermionic electron emitters. Its high-temperature surface chemistry and electrical properties have been exploited over the decades [20], and a few studies have been recently reported from the perspective of understanding the optical properties of LaB_6 nanoparticles, which exhibit plasmon resonance within the near-infrared (NIR) region [20-25]. It should also be noted that, to achieve a high NIR absorbance, a uniform dispersion of LaB_6 nanoparticles in a matrix is required, without which unstable optical performance will most likely occur [25].

Although the high-temperature stability of a LaB_6 crystal/electronic structure has been well established, there have been few reports focusing on the synthesis of pristine LaB_6 thin films [26-28] with specific characteristics such as high crystallinity and low loss, high optical response, thermal stability, and CMOS compatibility for plasmonic device applications. In this study, we demonstrate the synthesis of highly oriented LaB_6 films with low-loss and high optical response, having an optical figure of merit (FOM) closer to that of Au and better than those of W, Mo, and TiN [29-31]. We also estimate through simulation the absorption, scattering efficiency, electric field intensity, and reflectance spectra for LaB_6 nanostructures, which revealed similar optical characteristics between LaB_6 and Au. Furthermore, LaB_6 exhibited an excellent FOM compared to previously reported results for W, Mo, and TiN within the NIR region, and has demonstrated the best results thus far when applied to compound plasmonic materials.

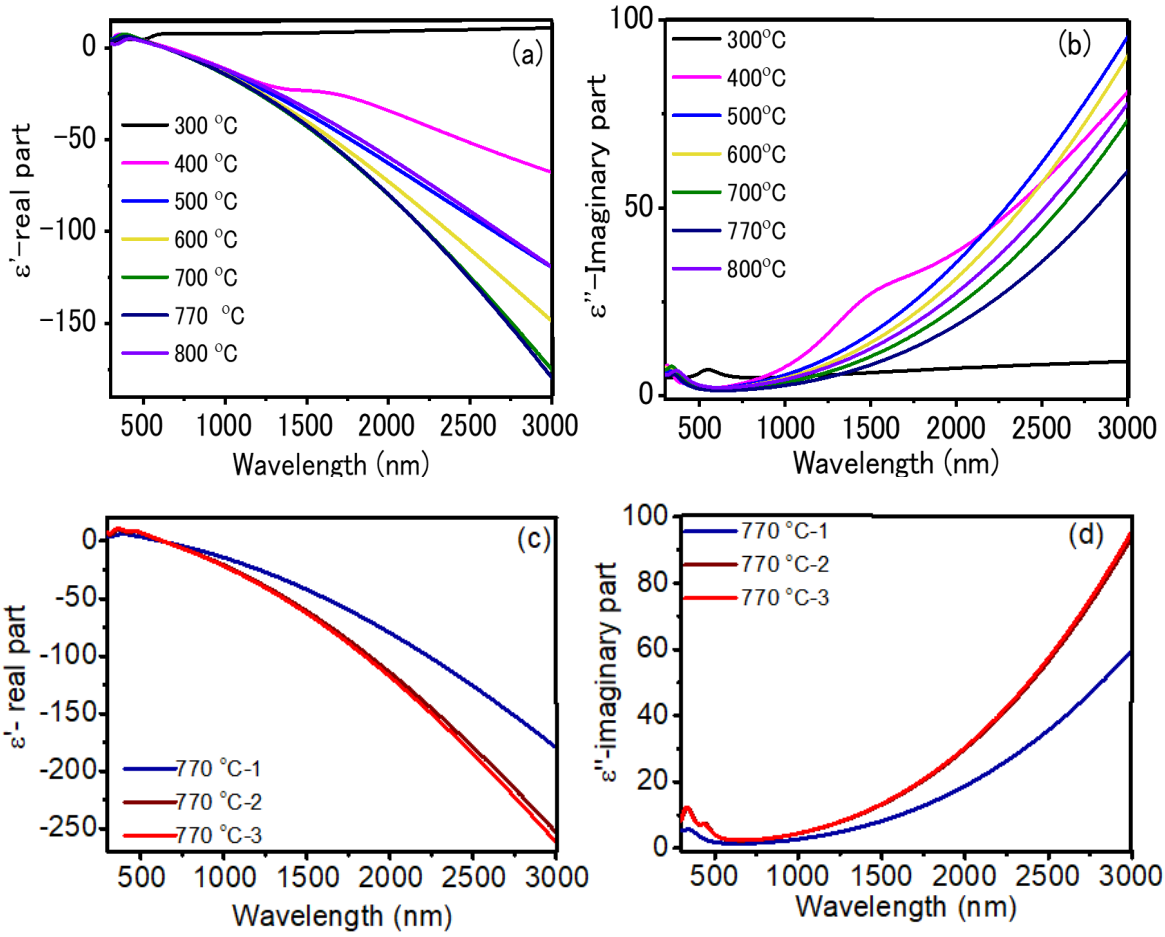

Figure 1. (a) Real and (b) imaginary parts of the complex permittivity of LaB_6 films deposited at different film growth temperatures with a deposition rate of 2.5 nm/s. (c) Real and (d) imaginary parts of the complex permittivity of LaB_6 films deposited at 2.5 nm/s (sample 770 °C-1), 2.5 nm/s (sample 770 °C-2), and 3.5 nm/s (sample 770 °C-3) at a fixed deposition temperature of 770 °C. Sample 770 °C-1 was deposited using a commercial sintered LaB_6 target, and samples 770 °C-2 and 770 °C-3 were deposited using high-purity single crystal LaB_6.

2 Results and Discussions

Figures 1(a)–1(d) show the dielectric functions (*i.e.*, real (ε') and imaginary (ε'') parts of the permittivity) of our LaB_6 films retrieved through spectroscopic ellipsometry (spectral range of 0.3–3 μm, with angles of incidence varied from 50° to 60° in 5° steps). The samples were fabricated through electron (e)-beam evaporation on Si (100) substrates with native oxides using a LaB_6 target. As shown in Figs. 1(a) and 1(b), the film deposition was carried out at the same deposition rate of 2.5 Å/s with substrate temperatures varied from 300 to 800 °C. The films deposited at a substrate temperature of 400 °C and higher exhibit excellent metallic behavior (the real part of the permittivity is negative) within the visible to NIR spectral

regions for wavelengths longer than ~630 nm. The real part of the permittivity becomes more negative with films deposited at higher substrate temperatures, and increasing the temperature beyond 800 °C then leads to a decrease in metallicity. Furthermore, we found that the loss (the imaginary part of permittivity) increases with the substrate temperature. For our E-beam evaporation method, we revealed an optimum deposition temperature of 770 °C for producing LaB_6 films with high metallicity (770 °C-1). In addition, we grew the films (770 °C-2 and 770 °C-3) using a high-purity single-crystalline LaB_6 ingot grown by applying a floating zone (FZ) method and deposited the films with different deposition rates at 770 °C (770 °C-2, 2.5 nm/s; and 770 °C-3, 3.5 nm/s). The accuracy of the extracted complex dielectric function of the LaB6 films obtained by ellipsometry fitting was ensured based on the agreement between the thicknesses extracted through ellipsometry and those measured using stylus profilometry (Table S1, supporting information), for which the errors were within 5%. Hall measurements were also conducted to evaluate the carrier concentrations and mobility, and showed good agreement with the highly metallic nature observed in the ellipsometry results. In general, bulk LaB_6 has a carrier concentration within the range of ~10^{22} cm^{-3}, and for our films, we observed a carrier concentration of ~1×10^{22} cm^{-3}. In addition, it was observed that the mobility (Table S1, supporting information) of the LaB_6 films increased as the film became more optically metallic, or as the value of ε' became more negative. We also determined that these properties, especially optical characteristics, did not change at a higher temperatures of 600 °C and under atmospheric conditions (data are shown in S4), unlike conventional plasmonic materials such as Au, Al, Mo, W, and TiN, indicating the suitability and advantages of this material for use in photothermal applications.

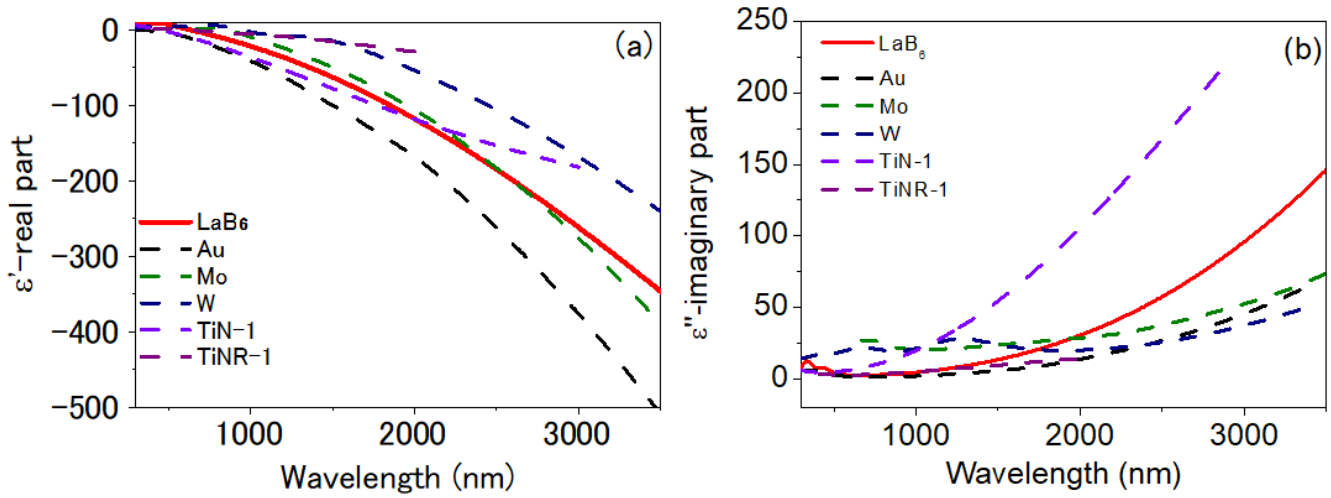

Figure 2. Comparison of the measured permittivity data from LaB_6 with those of Au, W, Mo, and TiN. (a) Real and (b) imaginary parts (permittivity data for TiN-R1 and TiN-R2 are extracted with permission from Refs. [14] (©2017 ACS) and [15] (©2017 AIP publishing). Permittivity data for Au are taken from Ref. [29]. Permittivity data for Mo and W are extracted from Refs. [30] and [31] for comparison.

For comparison, the permittivity data of LaB_6 films (770 °C-3) deposited through the E-beam deposition method are plotted along with data for conventional metals [14, 15, 30, 31] in Figs. 2(a) and 2(b). The figures clearly show that the real part of the permittivity of Au is more negative than that of all films shown in the comparison. Nonetheless, in the visible and NIR regions at up to ~1500 nm, our LaB_6 film shows values that are closer to those of Au, better than those of other refractory metals such as Mo and W, and slightly lower than the best reported value for TiN films. However, it should be noted that the imaginary part of LaB_6 is far lower than those of the Au, TiN, Mo, and W films, reflecting the low-loss characteristics of these high-quality LaB_6 films.

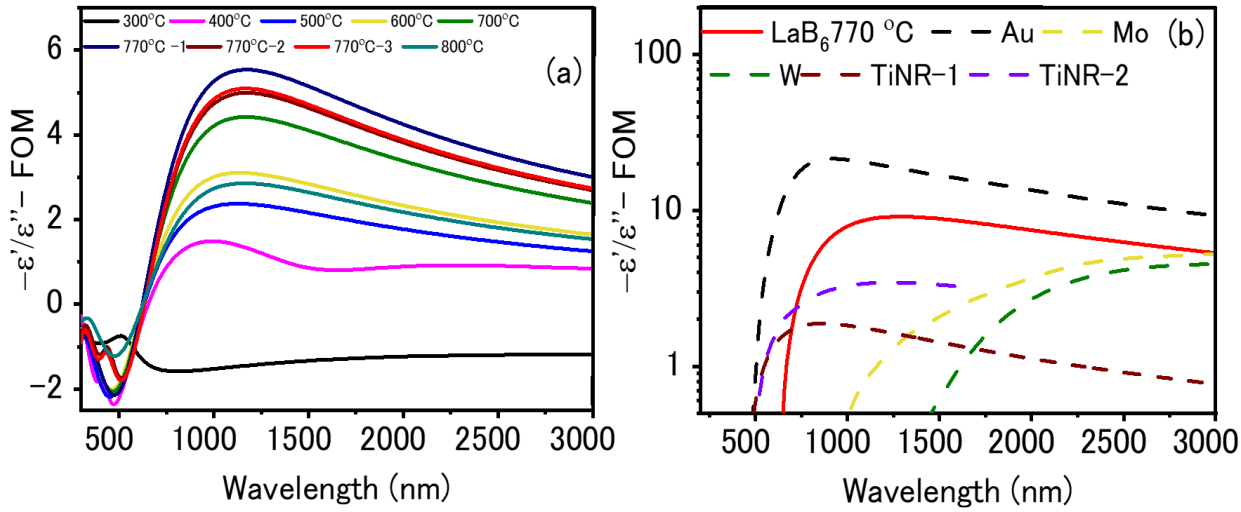

Figure 3. FOM -ε'/ ε'' for (a) LaB_6 grown at different substrate temperatures. (b) Best LaB_6 film (770 °C-3) in comparison with Au, W, Mo, and TiN (permittivity data for TiN-R1 and TiN-R2 are extracted with permission from Refs. [14] and [15]. Permittivity data of Au are taken from Ref. [29], whereas the permittivity data for Mo and W are extracted from Refs. [30] and [31] for comparison.

Figure 3(a) shows the FOM of different LaB_6 films at various substrate temperatures. The peak value was at approximately 1.2 μm for all films except the dielectric LaB_6 film deposited at 300 °C. The FOM for LaB_6 increases monotonically as the substrate temperature increases, and the grain size increases. The FOM value of the LaB_6 film grown at 770 °C is the highest among all the LaB_6 films. However, when the substrate temperature increases beyond 770 °C, the FOM slightly decreases, owing possibly to interdiffusion beginning to occur with the Si substrate at this temperature. Figure 3(b) shows a comparison of the FOM of the LaB_6 film (770 °C-3) with that of conventional metals and TiN. The FOM of LaB_6 is higher than that of conventional high-temperature metals such as Mo, W, and TiN, owing to its low-loss characteristics [16, 17, 30, 31]. This shows that LaB_6 could have practical application as a stable high-temperature plasmonic material within the visible to NIR region and with better performance than other high-temperature plasmonic materials [11, 13].

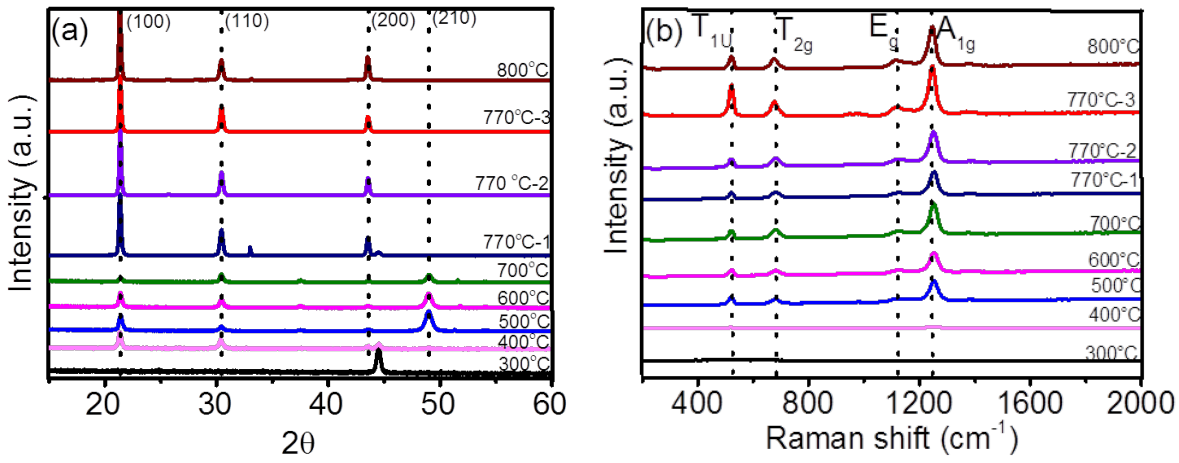

Figure 4. (a) XRD and (b) Raman spectra of LaB_6 films deposited at different substrate temperatures.

Figure 4(a) shows the X-ray diffraction (XRD) patterns of LaB_6 thin films deposited at various substrate temperatures and deposition rates. A crystalline structure inherent to LaB_6 is revealed in films with a substrate growth temperature above 400 °C, and the intensity of the (100) diffraction peak reaches the highest level for those films with higher substrate temperatures and for samples deposited with a higher rate of deposition at 770 °C. Smaller (110), (111), and (200) diffraction peaks are also detected in the LaB_6 films deposited at a higher substrate temperature. We also analyzed the average crystallite size based on Halder-Wagner analysis. The crystallite size was approximately 25–30 nm at 400 °C to 700 °C and increased to 40 nm at 770 °C, which correlates with the improved optical properties of LaB_6 films deposited at 770 °C. Figure 4(b) shows the Raman scattering spectra of LaB_6 thin films with varying substrate temperatures and deposition rates. Vibrational modes corresponding to the bending (T_{2g}) and stretching (E_g and A_{1g}) modes of the LaB_6 boron octahedron can be observed. Acoustic or T_{1u} modes with displacement of lanthanum atoms with respect to boron octahedral cages can be observed [26, 32, 33]. This mode is originally Raman inactive in bulk, but becomes Raman active herein, probably owing to the deformation and symmetry breaking of the near-surface lattices or at the grain boundaries. It can be observed that all LaB_6 Raman modes are present in the LaB_6 films deposited at substrate temperatures higher than 400 °C, whereas the film deposited at 300 °C exhibits only a dielectric nature and does not exhibit any LaB_6 Raman modes. This agrees with the XRD results, in which deposition at above 400 °C leads to the formation of crystalline LaB_6, and consequently, exhibits a strong metallicity, both electrically and optically, as we expected from its electronic structure.

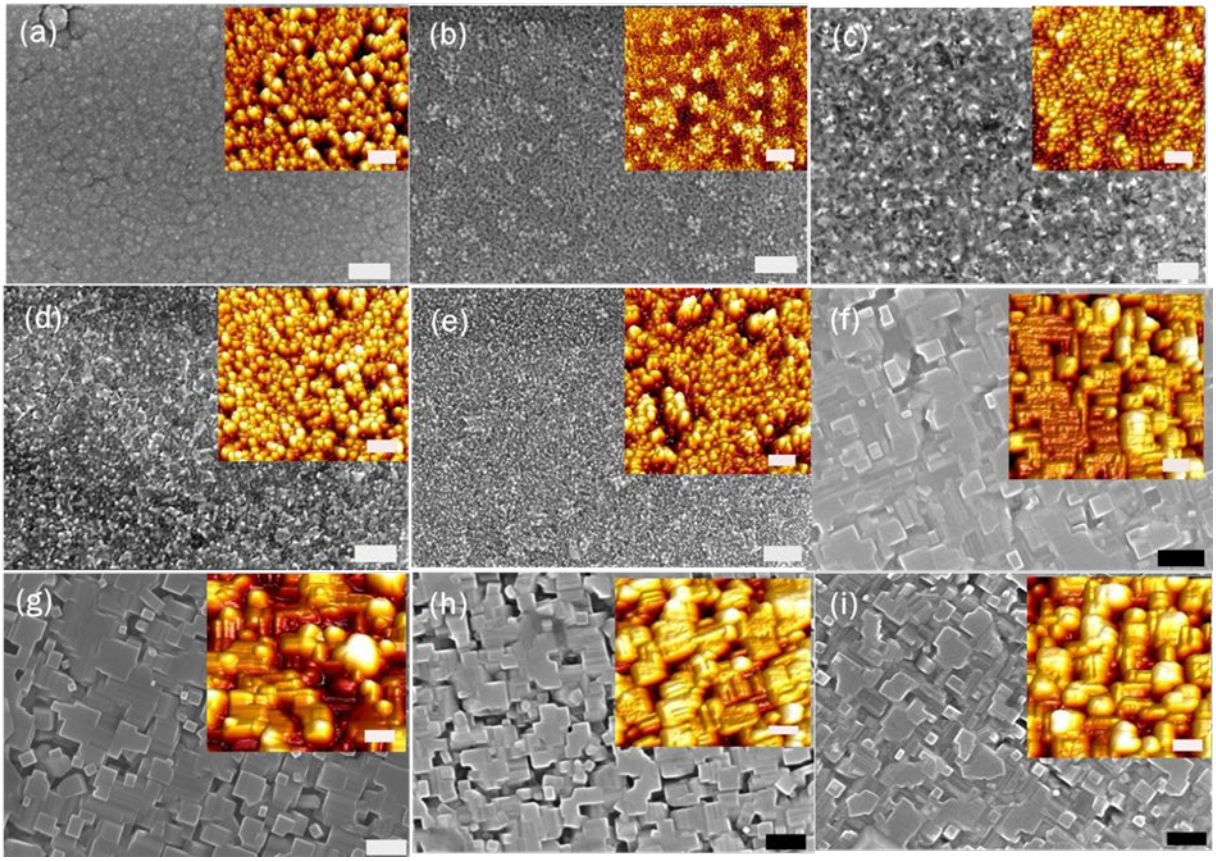

Figure 5. SEM images of LaB_6 films with different substrate temperatures: (a) 300 °C, (b) 400 °C, (c) 500 °C, (d) 600 °C, (e) 700 °C, (f), 770-1 °C (g), 770-2 °C (h), 770-3 °C, and (i) 800 °C with corresponding AFM images in the inset. The scale bars of the SEM and AFM images are 100 nm.

Figures 5(a)–5(i) show SEM images of LaB_6 at various substrate temperatures and deposition rates with the corresponding atomic force microscope (AFM) images in the insets. At 300 °C, it can be seen that small grains are uniformly distributed, and as the substrate temperature increases, there is a local clustering of grains. As the temperature reaches 770 °C, well-defined faceted crystallites with an average size of 40 nm are formed at different deposition rates. A sufficiently high substrate temperature provides efficient diffusion processes for the particles and leads to the growth of large crystallites with an excellent uniaxial (001) orientation and high coherency in the azimuthal orientation, as can be seen from the alignment in the edge orientation. A separate crystal growth study indicated that this coherence in the crystal orientation is motivated by epitaxial growth with a *magic mismatch* of the coincidence lattices of LaB_6 and Si(001) surface, which exhibits an in-plane azimuthal rotation of 45° with respect to each other (LaB_6[100]||Si [110]) [26].

As mentioned earlier, there have been very few reports on the optimization of pristine LaB_6 films for optical applications. Although the effect of substrate temperature has been investigated, improvement of the optical properties of LaB_6 has focused mainly on doping. Herein, we have shown a direct relationship between high crystallinity and better optical properties of LaB_6, rather than doping [27, 28]. In particular, we have demonstrated the evolution of the surface morphology and crystallite size with the substrate temperature and its clear effect on the optical properties of LaB_6. We have shown that LaB_6 can be plasmonic, starting from a substrate temperature as low as 400 °C. In addition, we have identified the optimum substrate temperature (770 °C), together with the effects of the deposition rate for LaB_6 films with excellent metallic/plasmonic behavior. Beyond this temperature, the possible interdiffusion of B and Si can degrade the crystallinity of LaB_6 [26]. This also agrees with our experimental results obtained at 800 °C, where a lower FOM can be observed when compared to the films deposited at 770 °C. In addition to E-beam evaporation, we attempted to deposit LaB_6 under similar conditions, except for a slower deposition rate through the pulsed laser deposition (PLD) technique, i.e., ~0.05 Å/s (Figs. S2 and S3, supporting information). However, the PLD deposited films were dielectric and nonmetallic, exhibiting a discontinuous nature as a consequence of the low deposition rate. This underlies the importance of the high deposition rate required for fabricating LaB_6 films with good metallic/plasmonic behavior, which can have an impact on device applications. Overall, our LaB_6 film deposited at 770 °C exhibited a low-loss nature and the best optical FOM, as discussed above, because of its increased grain size and lateral coherence between the grains.

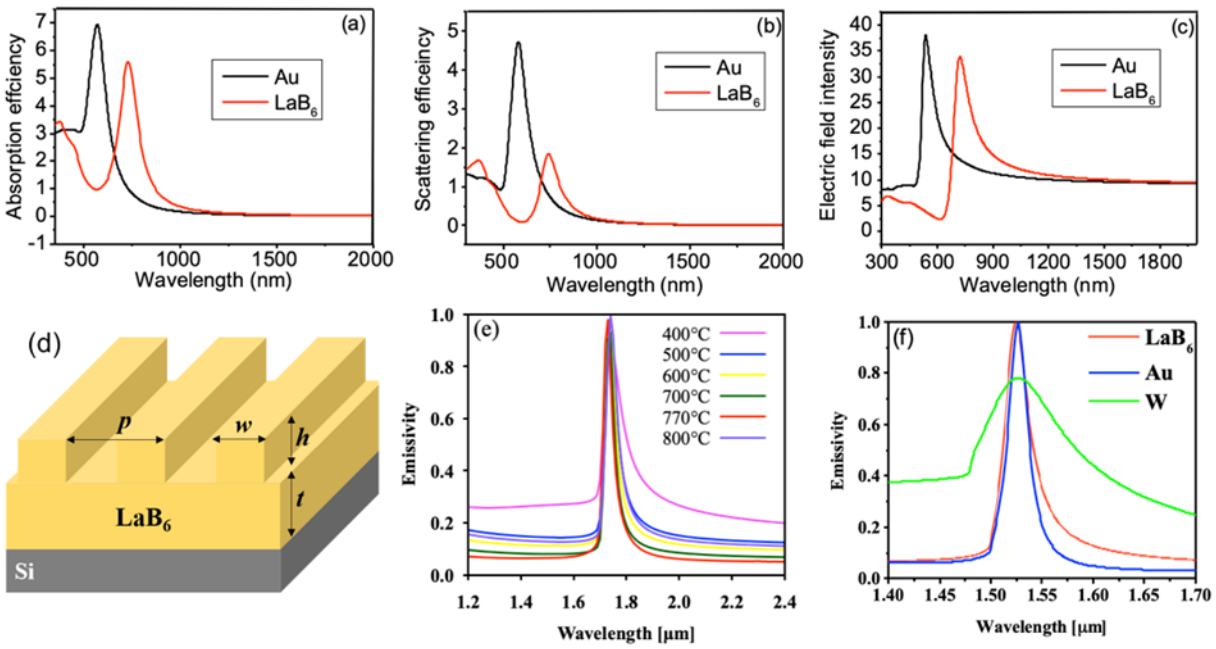

Figure 6. Analytically calculated (a) absorption and (b) scattering efficiencies of 50-nm radius spheres in water for LaB_6 and Au nanospheres. The permittivity of the LaB_6 (770 °C-3) from this study is adapted to this analysis. (c) Analytically calculated maximum near-field intensity around nanospheres made of LaB_6 and Au in a dipole approximation. (d) Schematic representation of LaB_6 arranged in a periodic 1D trench array (grating) on a Si substrate. (e) Influence of film deposition temperatures on the emissivity spectra of the LaB_6 1D grating thermal emitters. Geometry of the 1D grating is p = 1.7 μm, h = 0.1 μm, t = 0.2 μm, and w = 0.85 um. (f) Comparison of simulated emissivity of LaB_6 with Au and W using an identical grating structure. The performance of the LaB_6 device is comparable to that of the Au device.

To demonstrate the plasmonic properties of LaB_6, we compared its properties with those of Au in three representative configurations either analytically or numerically. Figures 6(a) and 6(b) show the analytically calculated absorption and scattering efficiencies of 50-nm radius spheres in water, respectively. The peak positions of the LaB_6 nanospheres are red-shifted compared to those of the Au nanospheres, whereas the peak heights are comparable. It can be observed that the bandwidth of the LaB_6 nanospheres is smaller than that of the Au nanospheres. It should also be noted that the LaB_6 nanospheres offer better performance (scattering and absorption) within the entire NIR region than the Au nanoparticles. Figure 6(c) shows the maximum field intensity at the nanosphere surface under the dipole approximation limit. Similar to cases with scattering and absorption efficiencies in the far field, the near-field intensities of the LaB_6 and Au nanospheres are nearly comparable within the visible region. However, the LaB_6 nanosphere shows better performance than Au within the NIR region ($\lambda > 780$ nm), and enters a biological

transparency window, where plasmonic hyperthermia medical applications are expected. The performance shown here is also better than all values reported for TiN, which has been widely studied in hyperthermia as well as in photothermal solar harvesting to replace expensive Au [11-15]. Moreover, this feature is useful for HAMR applications, where the use of complex nanoscale geometries is imminent.

Figures 6(d) and 6(e) show the schematic and simulated emissivity spectra (calculated based on the rigorous coupled-wave analysis method using Synopsys' RSoft) of LaB_6 1D grating arrays (on 100-nm thick films) with deposition temperatures varying from 400 ℃ to 800 ℃. Considering the narrowness of the emission peak widths and suppression of unwanted spectral background, it can be seen that LaB_6 deposited at 770 ℃ (red curve) exhibits the best performance. Furthermore, the change in the spectral background and peak width correlates well with the FOMs, as shown in Fig. 3(a). With an appropriate grating configuration, the strongly metallic and low-loss nature of our LaB_6 film can be utilized to realize tunable spectral emissivity with a sharp bandwidth and high emissivity, which is desirable for thermophotovoltaics and drying applications used in the industry.

Figure 6(f) shows a comparison of the simulated spectral emissivities of LaB_6, Au, and W with identical emitter structures. It should be noted that the bandwidth of the LaB_6 nanostructure is comparable to that of Au, which is the best plasmonic material, and better than that of W, which is the most frequently used refractory metal. Furthermore, LaB_6 films exhibit high-temperature stability of up to 800 °C in air, and the oxidation resistance is improved by approximately 400 °C in comparison to other high-temperature ceramics such as ITO and TiN [18, 34, 35], as we demonstrated, for example, in S4 and S5. The high-temperature stability indicates that the operating wavelength of the LaB_6 emitter can be within the NIR region, which makes the LaB_6 film ideal for designing a strong and sharp NIR absorption as well as a tunable narrow-band NIR emission [11, 12, 18, 37]. These features are advantageous compared to many other plasmonic thin films that are currently being investigated for high-temperature plasmonic device applications, such as spectroscopic thermal emitters [36, 38].

3 Summary

To summarize, we demonstrated the synthesis of highly oriented epitaxial LaB_6 thin films on a Si substrate using an E-beam deposition method. The film quality and its properties broadly change according to the substrate temperature by varying the grain size and coherency. It was established that deposition rates of above ~2 Å/s and a substrate temperature of higher than 400 ºC produce LaB_6 thin films with a large optical FOM, which is excellent for plasmonic applications in the NIR to mid-infrared region. The optical FOM of our film yields values far higher than those of W, Mo, and TiN, which lie closer to that of Au within the entire NIR as well as mid-infrared region. We also estimate that the

absorption/scattering/emission efficiencies, local electric field intensity, and bandwidth of the localized surface plasmon resonance and surface lattice resonance of LaB_6 are comparable to those of Au. Because LaB_6 exhibits higher mechanical and thermal stability and is more cost-effective than Au and Ag, it is considered to be an excellent practical plasmonic material that can replace both conventional elemental metals. Combined with excellent plasmonic properties and extreme thermal stability, as well as low work functions, we believe that metal hexaborides can open up a new area of research in which other plasmonic materials have yet to be realized for future energy applications.

Experimental Section

Fabrication: E-beam evaporation was applied at substrate temperatures of 300 °C and 800 °C in a vacuum of ~1×10^{-7} Torr. The deposition rate was varied between 2.5 and 3.5 A˚/s. The target-substrate distance was 20 cm. All films were deposited from a LaB_6 ceramic target on a heated Si (001) substrate. Two types of targets were used for the deposition: commercially available hot-pressed LaB_6 (99.9% purity), purchased from Fuuruchii Chemical Lab. Co., and our single-crystalline LaB_6 target, prepared using an FZ crystal growth method.

Characterization: The thickness of the films prepared at various rates of deposition was measured using a step profiler (Dektak 150, Veeco Instruments). Surface profile measurements were performed using an AFM (Bruker). The crystal structures of the films were determined using an XRD (Smart Lab, Rigaku). Spectroscopic ellipsometry measurements were made from the ultraviolet (UV) to NIR wavelength range (240–3000 nm) using a variable-angle spectroscopic ellipsometer (SE850DUV, SENTECH). A Drude-Lorentz model with a single Lorentz oscillator and Drude term was used in all fittings and consistently provided a good fit with ellipsometric measurements, and the thickness values were highly consistent with the surface profile measurements (within a 5% deviation). The carrier concentration was determined through Hall measurements conducted using a Resitest 8400 series (Toyo Corporation) in AC field Hall measurement mode [39].

References

1. H A Atwater. *Sci. Am*. 2007, **296**, 56–62.
2. S Lal, S Link, N J Halas. *Nat. Photon*. 2007, **1**, 641–648.
3. S McCall, P Platzman, P Wolff. *Phys. Lett. A* 1980, **77**, 381–383.
4. A Otto. *Vacuum* 1983, **33**, 797–802.

5. K Chen, T D Dao, S Ishii, M Aono, T Nagao. *Adv. Funct. Mater*. 2015, **25**, 6637–6643.
6. C V Hoang, M Oyama, O Saito, M Aono, T Nagao. *Sci. Rep*. 2013, **3**, 1175.
7. A Boltasseva, H A Atwater. *Science* 2011, **331**, 290–291.
8. G V Naik, V M Shalaev, A Boltasseva. *Adv. Mater*. 2013, **25,** 3264–3294.
9. M I Stockman. *Opt. Express* 2011, **19**, 22029–22106.
10. S L Shinde, S Ishii, T D Dao, R P Sugavaneshwar, T Takei, K K Nanda, T Nagao. *ACS Appl. Mater. Interfaces* 2018, **10** (3), 2460–2468.
11. J J Foley, C Ungaro, K Sun, M C Gupta, S K Gray. *Opt. Express* 2015, **23**, A1373–A1387.
12. Y Guo, S Molesky, H Hu, C L Cortes, Z Jacob. *Appl. Phys. Lett*. 2014, **105**, 073903.
13. S Ishii, R P Sugavaneshwar, T Nagao. *J. Phys. Chem. C* 2016, **120**, 2343–2348.
14. R P Sugavaneshwar, S Ishii, T D Dao, A Ohi, T Nabatame, T Nagao. *ACS Photonics* 2017 **5** (3), 814-819
15. J A Briggs, G V Naik, Y Zhao, T A Petach, K Sahasrabuddhe, D Goldhaber-Gordon, N A Melosh, J A Dionne. *Appl. Phys. Lett*. **110** (10), 101901 (2017).
16. A Lalisse, G Tessier, J Plain, G Baffou. *J. Phys. Chem. C* 2015, **119** (45), 25518–25528.
17. S Bagheri, C M Zgrabik, T Gissibl, A Tittl, F Sterl, R Walter, S De Zuani, A Berrier, T Stauden, G Richter, E. L Hu, H Giessen. *Opt. Mater. Express* 2015, **5** (11), 2625–2633.
18. T D Dao, A T Doan, D H Ngo, K Chen, S Ishii, A Tamanai, T Nagao. *Opt. Mater. Express* 2019, **9** (6), 2534–2544.
19. J M Lafferty. *J. Appl. Phys*. 1951, **22**, 299−309.
20. T M Mattox, A Agrawal, D J Milliron. *Chem. Mater*. 2015, **27**, 6620−6624.
21. S Schelm, G B Smith, P D Garrett, W K.Fisher. *J. Appl. Phys.* 2005, **97**, 124314.
22. C Chen, D Chen. *Chem. Eng. J.* 2012, **180**, 337–342.
23. H Takeda, H Kuno, K Adachi. *J. Am. Ceram. Soc*. 2008, **91**, 2897–2902.
24. K Machida, K Adachi. *J. Appl. Phys.* 2015, **118**, 013103.
25. T M Mattox, S Chockkalingam, I Roh, J J Urban. *J. Phys. Chem. C* 2016, **120**, 5188–5195.
26. Ø S Handegård, H D Ngo, R P Sugavaneshwar, A T Doan, N Furuhata, S Otani, T Nagao. *Appl. Phys. Express* 2020 **13** (5), 055504.
27. E Kafadaryan, S Petrosyan, G Badalyan, S Harutyunyan, A Kuzanyan. *Thin Solid Films* 2002, **416** (1-2), 218–223.
28. A Yutani, A Kobayashi, A Kinbara. *Appl. Surf. Sci*. 1993, **70**, 737–741.
29. R L Olmon, B Slovick, T W Johnson, D Shelton, S H Oh, G D Boreman, M B Raschke. *Phys. Rev. B* 2012, **86**, 235147.
30. M A Ordal, R J Bell, R W Alexander, L A Newquist, M R Querry. *Appl. Opt*. 1988, **27**, 1203–1209.
31. A D Rakić, A B Djurišić, J M Elazar, M L Majewski. *Appl. Opt*. 1998, **37**, 5271–5283.
32. T Nagao, T Kitamura, T Iizuka, M Umeuchi, C Oshima, S Otani. *Surf. Sci.* 1993, **287**, 391–395.

33. T Nagao, K Kitamuara, Y Iizuka, C Oshima, S Otani. *Surf. Sci.* 1993, **290** (3), 436–444.
34. C.-H Wen, T.-M Wu, C J Wei. *J. Eur. Cer. Soc*. 2004, **24** (10-11), 3235–3243.
35. J Sonber, K Sairam, T. C Murthy, A Nagaraj, C Subramanian, R Hubli. *J. Eur. Cer. Soc*. 2014, **34** (5), 1155–1160.
36. T Yokoyama, T D Dao, K Chen, S Ishii, R P Sugavaneshwar, M Kitajima, T Nagao. *Adv. Opt. Mater*. 2016, **4** (12), 1987–1992.
37. T D Dao, K Chen, S Ishii, A Ohi, T Nabatame, M Kitajima, T Nagao. *ACS Photonics* 2015 **2** (7), 964–970.
38. T M Mattox, J. J. Urban. *Materials* 2018, **11** (12), 2473.
39. D K Schroder. Semiconductor Material and Device Characterization, John Wiley & Sons, New York, 1990.

Acknowledgments

This work was supported in part by JSPS KAKENHI (Grant No. 16H06364).

Supporting Information

Supporting Information is available from the Wiley Online Library or from the author.